Atmospheric bending effects in GNSS tomography

Gregor Möller[1] and Daniel Landskron[1]

[1]Department of Geodesy and Geoinformation, Vienna University of Technology, Vienna, Austria

Correspondence: Gregor Möller (gregor.moeller@tuwien.ac.at)

Abstract. In GNSS tomography, precise information about the tropospheric water vapor distribution is derived from integral measurements like GNSS slant wet delays (SWDs). Therefore, the functional relation between observations and unknowns, i.e. the signal paths have to be accurately known for each station-satellite pair involved. Since GNSS signals are prone to atmospheric bending effects, a straight line assumption is not sufficient for elevation angles $< 15°$. Thus, in the following, a
5 mixed 2D piecewise linear ray-tracing approach is introduced and possible error sources in reconstruction of the bended signal paths are analyzed in more detail. Especially, if low elevation observations ($\varepsilon < 10°$) are considered, unmodeled bending effects can introduce a systematic error of up to $10 - 20 ppm$, on average of $1 - 2 ppm$ into the tomography solution. Thereby, the ray-tracing approach itself but primarily the quality of the a priori field has a significant impact on the reconstruction quality. In order to overcome possible limitations in the a priori field, an iterative tomography processing strategy is applied.
10 Further, a bending model helps to reduce the number of processing steps by up to 85%. In consequence, the developed mixed ray-tracing approach allows not only for a correct treatment of low elevation observations but is also fast and applicable for near real-time applications.

1   Introduction

For conversion of precise integral measurements into two- or three-dimensional structures, a technique called tomography has
15 been invented. In the field of GNSS meteorology, the principle of tomography became applicable with the increasing number of GNSS satellites and the build-up of densified ground-based GNSS networks in the 1990s (Raymond et al., 1994; Flores, 1999). According to Iyer and Hirahara (1993), the general principle of tomography is described as follows:

$$f_s = \int\limits_S g_s \cdot ds \tag{1}$$

where f_s is the projection function, g_s is the object property function and ds is a small element of the ray path S along which
20 the integration takes place. In GNSS meteorology, g_s is usually replaced by refractive index $n - 1$, and integral measure f_s by the GNSS signal delay in the neutral atmosphere (STD)

$$STD = \int\limits_R n \cdot ds - \int\limits_S ds \tag{2}$$

where R is the true signal path and S is the theoretical straight-line signal path in vacuum. A full non-linear solution for the refractive index n is not of practical relevance since according to Fermat´s principle, first order changes of the ray path lead to

second order changes in travel time. In consequence, by ignoring the path dependency in the inversion of n along ds and by assuming the ray path as a straight line, a linear tomography approach can be defined which is well applicable to $STDs$ above $15°$ elevation angle (Möller, 2017). However, with decreasing elevation angle, the true signal path deviates significantly from a straight line. In consequence, by ignoring atmospheric bending, a systematic error is introduced in the tomography solution.

5 In order to overcome this limitation, in the following an *iterative tomography approach* is defined in which the bended signal path is approximated by small line segments. Similar to the linear tomography approach, thereby the neutral atmosphere or parts of it are discretized in volume elements (voxels) in which the refractivity $N_k = (n_k - 1) \cdot 10^6$ in each voxel k is assumed as constant. Consequently, Eq. (2) can be replaced by:

$$STD = \sum_{k=1}^{m} N_K \cdot d_k \qquad (3)$$

10 where d_k is the travelled distance in each voxel. Assuming l observations and m voxels, a linear equation system can be set up. In matrix notation it reads:

$$\boldsymbol{STD} = \boldsymbol{A} \cdot \boldsymbol{N} \qquad (4)$$

where $\boldsymbol{STD}$ is the observation vector of size $(l, 1)$, $\boldsymbol{N}$ is the vector of unknowns of size $(m, 1)$ and $\boldsymbol{A}$ is a matrix of size (l, m) which contains the partial derivatives of the slant total delays with respect to the unknowns, i.e. the travelled distances d_k in
15 each voxel.

$$\boldsymbol{A} = \begin{bmatrix} \frac{\delta STD_1}{\delta N_1} & \cdots & \frac{\delta STD_1}{\delta N_m} \\ \vdots & \ddots & \vdots \\ \frac{\delta STD_l}{\delta N_1} & \cdots & \frac{\delta STD_l}{\delta N_m} \end{bmatrix} \qquad (5)$$

In case of slant wet delays ($SWDs$), Eq. (4) can be rewritten as follows:

$$\boldsymbol{SWD} = \boldsymbol{A} \cdot \boldsymbol{N_w} \qquad (6)$$

where $\boldsymbol{N_w}$ contains the wet refractivities in each voxel. In case a priori information ($\boldsymbol{N_{w0}}$) can be made available, it enters the
20 least squares tomography solution as follows:

$$\boldsymbol{N_w} = \boldsymbol{N_{w0}} + \boldsymbol{V} \cdot \boldsymbol{S}^{-1} \cdot \boldsymbol{U}^T \cdot \boldsymbol{A}^T \cdot \boldsymbol{P} \cdot (\boldsymbol{SWD} - \boldsymbol{A} \cdot \boldsymbol{N_{w0}}) \qquad (7)$$

where matrix $\boldsymbol{U}$, $\boldsymbol{V}$ and $\boldsymbol{S}$ are obtained by singular value decomposition of matrix $\boldsymbol{A}^T \cdot \boldsymbol{P} \cdot \boldsymbol{A} + \boldsymbol{P_c}$. For further details, the reader is referred to Möller (2017). In order to determine $\boldsymbol{N_w}$, weighting matrices $\boldsymbol{P}$ and $\boldsymbol{P_c}$ but also the travelled distances d_k in each voxel have to be determined. While in most tomography approaches observations gathered at low elevation angles are
25 discarded (Bender et al., 2011; Champollion et al., 2005; Hirahara, 2000), straight-line signal path reconstruction is sufficient for the determination of the paths lengths. However, a correct tomography solution based on low elevation observations is longing for more advanced ray-tracing algorithms. The first paper which deals with bended ray path reconstruction in GNSS

tomography was published by Aghajany and Amerian (2017), who compared different ray-tracing approaches and briefly analyzed its impact on the tomography solution.

   In the following, a more detailed discussion of possible error sources in signal path reconstruction is provided. Therefore, Sect. 2 describes the effect of atmospheric bending and its handling in GNSS signal processing. Section 3 deals with the

5   reconstruction of signal paths using ray-tracing techniques. Hereby, the modified piecewise linear ray-tracing approach is introduced - including its ability for reconstruction of the GNSS signal geometry. In Sect. 4, the defined ray-tracing approach is applied to real SWDs and its impact on the tomography solution is assessed and validated against radiosonde data. Section 5 concludes the major findings.

2   Atmospheric bending effects in GNSS signal processing

10   The effect of atmospheric bending on GNSS signals is related to the propagation properties of electromagnetic waves. In vacuum, GNSS signals travel with the velocity of light. When entering into the atmosphere, the electromagnetic wave velocity changes, dependent on the electric permittivity (ϵ) and magnetic permeability (μ) of the atmospheric constituents and the frequency of the electromagnetic wave. The ratio between the velocity of light c in vacuum and the velocity ν in a medium defines the refractive index n.

15   $$n = \frac{c}{\nu} = \sqrt{\frac{\epsilon \cdot \mu}{\epsilon_0 \cdot \mu_0}} \tag{8}$$

For signals in the microwave frequency-band, n ranges usually from 0.9996 to 1.0004, which goes along with a wave velocity slightly higher or lower than the velocity of light.

$$n_i \cdot \sin \Theta_i = n_0 \cdot \sin \Theta_0 \tag{9}$$

In consequence and according to Eq. (9), the electromagnetic wave experiences thereby a curvature effect (change in angle of

20   incidence Θ for $\Theta_0 \neq 0$), also known as atmospheric bending. In GNSS signal processing both effects, the change in velocity but also the deviation of the signal path from a straight line, have to be taken into account since both cause a change in atmospheric signal travel time ($\Delta\rho$).

$$\Delta\rho = \frac{1}{c} \cdot \left[\int_R n \cdot ds - \int_R ds \right] + \frac{1}{c} \cdot \left[\int_R ds - \int_S ds \right] \tag{10}$$

The first term of Eq. (10) describes the change in travel time due to velocity changes along the true ray path R. The second

25   term (about three orders of magnitude smaller than the first term) is related to the difference in geometrical path length between the true (R) and the chord signal path (S). However, in most GNSS applications not the true signal path but rather its impact on the signal travel time is modelled – separately for neutral troposphere (Bevis et al., 1992) and ionosphere (Fritsche et al., 2005). For highest precision, the GNSS signal delay in the neutral atmosphere or parts of it on top of an a priori model are estimated together with other parameters of interest using Eq. (11). Therefore, the STD is split into three components, namely

hydrostatic, wet and asymmetric delay:

$$STD(\varepsilon, \alpha) = ZHD \cdot mf_h(\varepsilon) + ZWD \cdot mf_w(\varepsilon) + G(\varepsilon, \alpha) \tag{11}$$

where ZHD is the zenith hydrostatic delay, ZWD is the zenith wet delay and mf_h and mf_w are the corresponding mapping functions, which describe the elevation (ε) dependency of the signal delay. The first-order horizontally asymmetric term $G(\varepsilon, \alpha)$ reflects local variations in the atmospheric conditions; see MacMillan (1995), Chen and Herring (1997) or Landskron and Böhm (2018). In practice, e.g. when using VMF1 mapping function (Böhm et al., 2006a) or similar mapping concepts, the tropospheric delay due to atmospheric bending is absorbed by the hydrostatic mapping function term mf_h. Comparisons between ray-traced $SHD(\varepsilon)$ and 'mapped' $SHD(\varepsilon) = ZHD \cdot mf_h(\varepsilon)$ slant hydrostatic delays reveal that about 97 % of the atmospheric bending effect is compensated by the VMF1 hydrostatic mapping function (see Appx. A for further details).

3   Reconstruction of GNSS signal paths

Assuming that the geometrical optics approximation is valid and that the atmospheric conditions change only inappreciably within one wavelength, the signal path is well reconstructible by means of ray-tracing shooting techniques (Hofmeister, 2016; Nievinski, 2009). Thereby, the basic equation for ray-tracing, the so-called Eikonal equation, has to be solved for obtaining optical path length L.

$$||\nabla L||^2 = n(\boldsymbol{r})^2 \tag{12}$$

From Eq. (12), a number of 3D and 2D ray-tracing approaches have been derived (Hobiger et al., 2008a). In order to find the optimal approach for operational analysis, Hofmeister (2016) carried out a number of exploratory comparisons. Based on the outcome, the 2D piecewise linear ray-tracer was defined as the optimal reconstruction tool for the iterative reconstruction of the atmospheric signal delays including atmospheric bending. It is fast and almost as accurate as the 3D ray-tracer, however for application in GNSS tomography, the ray-tracing approach had to be further modified. In the following, the developed mixed ray-tracing approach but also its impact on the GNSS tomography solution are discussed in more detail.

3.1   Piecewise linear ray-tracer

The starting point for the 2D piecewise linear ray-tracer is the receiver position in ellipsoidal coordinates $(\varphi_1, \lambda_1, h_1)$, the 'outgoing' elevation angle ε_k and the azimuth angle α under which the satellite is observed. In case of GNSS signals, both angles can be determined with sufficient accuracy from satellite ephemerides. In consequence, the initial parameters for ray-tracing (see Fig. 1), i.e. the geocentric coordinates (y_1, z_1) and the corresponding geocentric angles (η_1, θ_1) read:
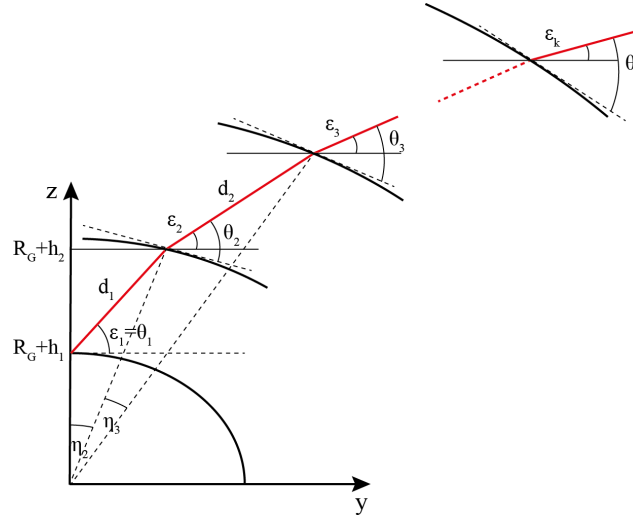
$$y_1 = 0 \tag{13}$$

$$z_1 = R_G + h_1 \tag{14}$$

Figure 1. Geometry of the ray-tracing approach with the geocentric coordinates (y, z), the geocentric angles (η, θ), elevation angle ε and d as the distance between two consecutive ray points

$$\eta_1 = 0 \tag{15}$$

$$\theta_1 = \varepsilon_k \tag{16}$$

where R_G is the Gaussian radius, an adequate approximation of the Earth radius

$$R_G = \frac{a^2 \cdot b}{(a \cdot \cos\varphi_1)^2 + (b \cdot \sin\varphi_1)^2} \tag{17}$$

with a and b as the semi-axes of the reference ellipsoid (e.g. GRS80). The z-axis connects the geocenter with the starting point, the y-axis is defined perpendicular to the z-axis in direction (azimuth angle) of the GNSS satellite in view. After setting the initial parameters, the 'true' ray path is reconstructed iteratively within two nested loops. In the *outer loop*, the meteorological parameters or total refractivity fields from an a priori field are read in and pre-processed for the inner loop. Therefore, the input data is interpolated vertically and horizontally to the vertical plane, spanned by the y- and z-axis. In the *inner loop*, for each height layer h_{i+1} with $i = 1 : (t-1)$ where t defines the top layer of the voxel model, the geocentric coordinates and the corresponding angles are computed as follows:

$$y_{i+1} = y_i + d_i \cdot \cos\varepsilon_i \tag{18}$$

$$z_{i+1} = z_i + d_i \cdot \sin\varepsilon_i \tag{19}$$

$$\eta_{i+1} = \arctan\frac{y_{i+1}}{z_{i+1}} \tag{20}$$

$$\theta_{i+1} = \arccos\left(\frac{n_i}{n_{i+1}} \cdot \cos(\theta_i + \eta_{i+1} - \eta_i)\right) \tag{21}$$

$$d_i = -(R_G + h_i) \cdot \sin\theta_i + \sqrt{(R_G + h_{i+1})^2 - (R_G + h_i)^2 \cdot \cos^2\theta_i} \tag{22}$$

5

$$\varepsilon_{i+1} = \theta_{i+1} - \eta_{i+1} \tag{23}$$

where d_i is the reconstructed path length between height layer h_i and h_{i+1} ($h_{i+1} > h_i$). It depends on the observation geometry but also on the atmospheric conditions (refractive indices n_i and n_{i+1}). By default, for our analysis, the spacing between two height layers h_i and h_{i+1} was set to 5 m, which corresponds to a maximum path length d_i of 100 m - assuming an outgoing

10   elevation angle of $3°$ ($5m/\sin3°$). The inner loop is repeated until the ray reaches the top layer t of the voxel model. Assuming spherical trigonometry, the spherical coordinates ($\varphi_{i+1}, \lambda_{i+1}$) of the ray path segments follow by Eqs. (24) and (25) to:

$$\varphi_{i+1} = \arcsin\left(\sin\varphi_1 \cdot \cos(\eta_{i+1} - \eta_1) + \cos\varphi_1 \cdot \sin(\eta_{i+1} - \eta_1) \cdot \cos\alpha\right) \tag{24}$$

$$\lambda_{i+1} = \lambda_1 + \arctan\left(\frac{\sin\alpha}{\cot(\eta_{i+1} - \eta_1) \cdot \cos\varphi_1 - \sin\varphi_1 \cdot \cos\alpha}\right) \tag{25}$$

15   where φ_{i+1} and λ_{i+1} are defined in the range $[-\pi/2, \pi/2]$ and $[-\pi, \pi]$, respectively. The ray coordinates are necessary for interpolation of the a priori refractive indices n_i and n_{i+1} for the next processing step i but also for computation of the intersection points with the voxel model boundaries.

The inner loop is repeated until $\varepsilon_t - \varepsilon_k + g_{bend}$ is smaller than a predefined threshold (e.g. 10^{-6} degrees). While the elevation angle ε_t is obtained by Eq. (23) for $i = t-1$, the correction term g_{bend} accounts for the additional bending above the top layer of

20   the voxel model. Since atmosphere is almost in state of hydrostatic equilibrium, g_{bend} can be well approximated by a bending model, like the one of Hobiger et al. (2008a):

$$g_{bend}[°] = \frac{0.02 \cdot \exp^{\frac{-h}{6000}}}{\tan\varepsilon_k} \tag{26}$$

where h is replaced by the height h_t of the voxel top layer. After convergence of the inner loop, the path length in each voxel is obtained by summing up the distances d_i in each voxel. Thereby, allocation of the ray parts is carried out by comparison of

25   the ray coordinates ($\varphi_i, \lambda_i, h_i$) with the coordinates of the voxel model. The obtained ray paths in each voxel - for each station and each satellite in view - are used for setting up design matrix $\boldsymbol{A}$ (see Eq. 5).

3.2 Quality of reconstructed ray paths

3.2.1 The a priori refractivity field

The quality of the ray-traced signal paths depends primarily on the quality of the a priori refractivity field. Especially if

30   no good a priori data can be made available, e.g. if standard atmosphere (StdAtm) is used instead of numerical weather model data (ALARO), the reconstructed signal path might deviate significantly from the 'true' signal path. Figure 2 shows the
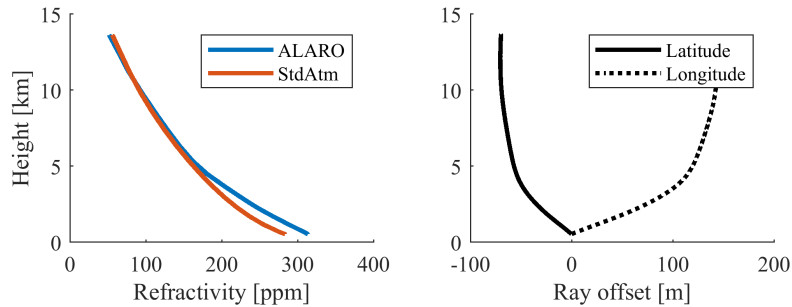
Atmospheric
Measurement
Techniques
Open Access
EGU
Discussions

Figure 2. Ray-traced signal path differences (right) caused by differences in the a priori refractivity field (left)

impact of the a priori refractivity field on the signal path, exemplary for a GNSS signal observed at station Jenbach, Austria $(\varphi = 47.4°, \lambda = 11.8°, h = 545m)$ at an elevation angle of $5°$. At this particular epoch (May 4, 2013, 15 UTC), standard atmosphere deviates by about 30 ppm from the ALARO model data. Assuming that the ALARO data is correct, ray-tracing through standard atmosphere causes a ray deviation of 100-200 m (see Fig. 2, right). In consequence, the reconstructed signal travels significantly apart from the observed signal. In order to reduce the impact of possible a priori refractivity errors on the reconstructed ray-paths and in further consequence on the tomography solution, the tomography processing was carried out iteratively, i.e. the first refractivity field obtained by solving Eq. (7) for N_w is used as a priori field for the next iteration. The processing is repeated until N_w converges.

Figure 3 shows the convergence behavior for two tomography solutions, which differ only with respect to the a priori refractivity field. Hereby, bias and standard deviation of the differences in N_w between two consecutive solutions were selected as convergence criteria. In case of good a priori data, two iterations are usually sufficient for $1ppm$-accuracy. Otherwise, e.g. when using standard atmosphere as a priori information, at least one iteration more is recommended. The adequate number of iterations depends also on the constraints applied to the a priori refractivity field. In case of too tight constraints, the number of iterations increases.

3.2.2 The empirical ray-bending model

Besides the a priori refractivity field, the quality of the reconstructed ray paths might be also affected by errors in the bending model, see Eq. (26). Comparisons of the bending model with ray-traced bending angles on a global $10° x 10°$ grid over the period of one year reveal that the error in bending is usually kept below 0.8 arcsec, see Fig. 4. Assuming a GNSS site near sea-level and an elevation angle of $5°$, an error in bending angle of ± 0.8 arcsec causes an error in path length of up to $\pm 10m$, i.e. the reconstructed GNSS signal enters the voxel model slightly earlier or later than the observed GNSS signal. However, for the tomography solution this effect is too small to be significant. In consequence, the bending model of Hobiger et al. (2008a) is well applicable for reconstruction of the bending angle above the voxel model, in particular if the voxel model height h_t is set to 12 km or higher.
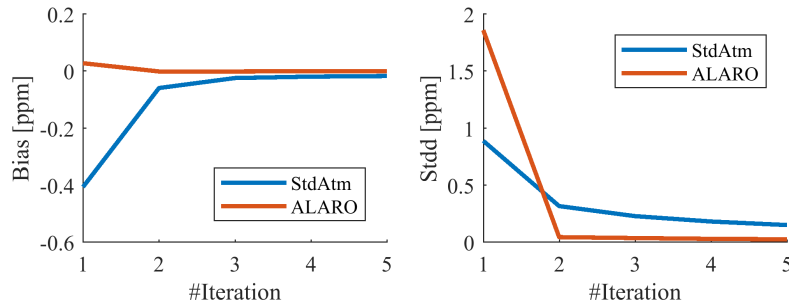
Figure 3. Bias (left) and standard deviation (right) of the differences in N_w between two consecutive tomography solutions- calculated separately for standard atmosphere and ALARO numerical weather model data as a priori refractivity field
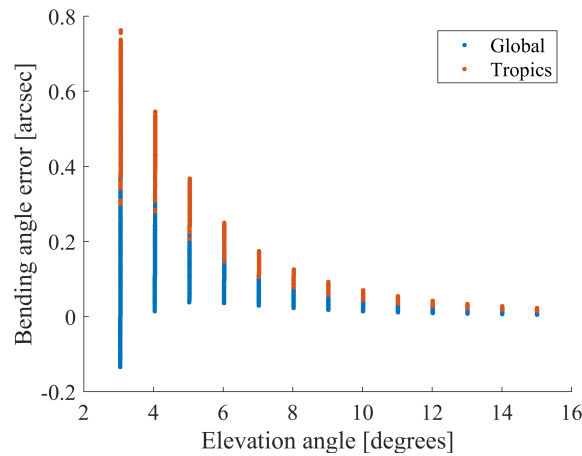

Figure 4. Error in bending angle caused by the bending model of Hobiger et al. (2008a) for $h = 12km$ (above the voxel model) - computed on a global $10° x 10°$ grid over the period of one year, 2014 by comparison with ray-traced bending angles based on ECMWF analysis data

3.2.3 Ionospheric bending effects

Beyond, also the ionosphere influences GNSS signal propagation. In order to assess the impact of free electrons in the ionosphere (above 80 km altitude) on the signal path, the electron density model by Anderson et al. (1987) was executed in three scenarios, assuming a vertical total electron content ($VTEC = \int N_e \cdot dh$) of 34 TECU (average daytime), 120 TECU (solar maximum) and 455 TECU (maximum possible, see Wijaya, 2010), respectively.

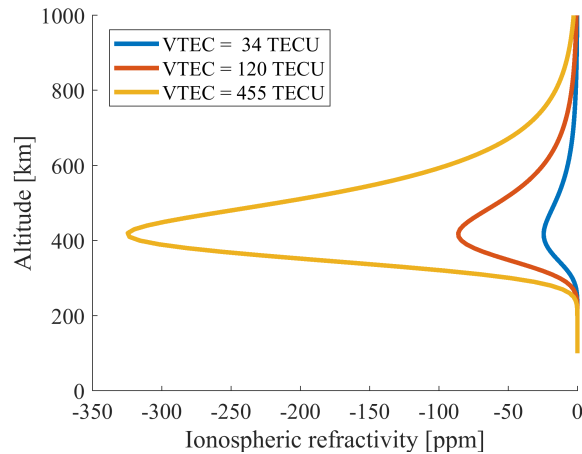$$N(f) = 10^6 \cdot \frac{-40.2993 \cdot N_e}{f^2} \tag{27}$$

Figure 5. Profiles of ionospheric refractivity $N(f)$ assuming signal-frequency $f = 1575.42MHz$

By making use of Eq. (27), the obtained electron density profiles were converted into profiles of refractivity (N), assuming signal frequency $f_1 = 1575.42MHz$ (GPS L1) and $f_2 = 1227.60MHz$ (GPS L2). Figure 5 shows the obtained vertical profiles of ionospheric refractivity, exemplary for frequency f_1. The higher the signal-frequency f the lower the phase velocity through the ionosphere and the less is its refraction. Following the approach by Wijaya (2010), the ray paths in the ionosphere were reconstructed, separately for GPS L1 and L2. The analysis revealed significant path differences between the 'true' ray path and its chord line but also between the two signal-frequencies. Assuming a VTEC of 455 TECU and an elevation angle of 3°, the maximum deviation from the straight-line signal path is 800 m for L1 and 550 m for L2 respectively, at $h = 400km$, slightly below the layer of peak electron density. Fortunately, ray path deviation decreases significantly with decreasing VTEC and altitude to a few tens of meters at $h = 12km$ (the upper rim of the troposphere at which the top of the voxel model is usually defined). In consequence, the impact of free electrons on the signal path in the lower atmosphere is negligible under moderate and low ionospheric conditions.

4 Impact of atmospheric bending on the tomography solution

In the following, the differences between straight line and bended ray-tracing are further analyzed. For highest consistency, the ray-tracing approach defined in Sect. 3 was used for both, straight line and bended ray-tracing. The only difference is that in case of straight line ray-tracing the ratio n_i/n_{i+1} in Eq. (21) was set to '1'. Thereby, it can be guaranteed that only the impact of atmospheric refraction is assessed.

In the beginning, the ray position is equal for both methods but diverges with increasing height. Thereby, the bended ray is travelling in most cases 'above' the straight ray, i.e. the straight ray enters the voxel model top 'earlier' than the bended ray. This leads to the effect that the straight ray remains longer in the voxel model than the bended ray, i.e. the straight ray path within the voxel model ($h < 13.6km$) is systematically longer than the bended ray path. The differences between both ray

Atmospheric
Measurement
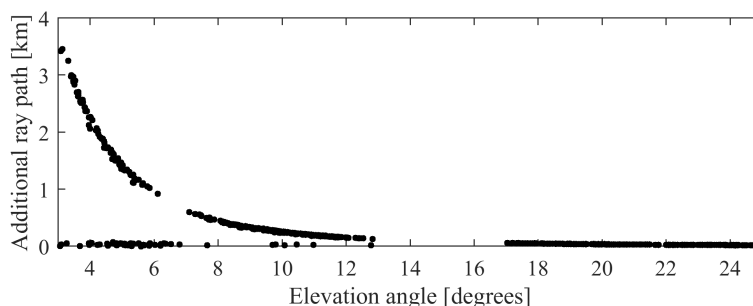Techniques
Discussions

Figure 6. Additional ray path caused by straight line ray-tracing

paths are plotted in Fig. 6 as function of elevation angle. Therefore, ALARO model data was selected as input for the bended ray-tracer. The additional ray path decreases rapidly with increasing elevation angle. Thus, a *mixed ray-tracing* approach can be defined, which considers ray bending only for $\varepsilon \leq 15°$. Beyond, the additional ray path is below 0.1 km, and straight line ray-tracing is sufficient for ray path reconstruction.

5   Figure 6 shows also that in some cases even for low elevation angles the difference in path length is small (below 0.1 km). This appears when the ray enters the voxel model not through the top layer but through a later surface of the voxel model. In this particular case the difference in path length between both ray-tracing approaches is negligible (be aware that only the entire distance through all voxels is comparable for both ray-tracing approaches but not the individual distances in each voxel).

        In order to study the impact of bended ray-tracing on the tomography solution, a GNSS tomography test case was defined.
10   The corresponding settings are summarized in Table 1. Figure 7 (left) shows the differences in wet refractivity obtained for the GNSS tomography test case on May 4, 2013, 15 UTC, whereby voxel number '1' is dedicated to the South-West corner and number '20' to the North-East corner of the voxel model. Between the voxels a bilinear interpolation method was applied. Even though on average over all voxels no bias in wet refractivity is observed, specific voxels show differences in wet refractivity of up to 12 ppm, particularly if due to bending different voxels than in the straight line solution are traversed. Figure 7 (right) shows
15   the differences in wet refractivity between two consecutive tomography solutions based on the mixed ray-tracing approach (Sol2, see Table 1). For Figure 7 (left) the a priori model was replaced by the improved wet refractivity field of the first solution (iterative solution). In this particular case, refractivity differences of up to 0.5 ppm are visible which implies that the a priori model used for the first solution is already close to the 'true' atmospheric conditions, i.e. in this particular case no further iteration was necessary. From all differences in wet refractivity over 248 epochs in May 2013, a maximum of $15.6ppm$, a bias
20   of $0.08ppm$ and a standard deviation of $0.2ppm$ were obtained. Although the bias and standard deviation over all voxels is small, differences of about $1ppm$ were observed on average at each epoch, especially when observations below $10°$ enter the tomography solution.

Atmospheric
Measurement
Techniques
Discussions

Open Access

Table 1. Summary of GNSS tomography test case settings

| Parameter	Settings
Period	May 2013, 8 epochs per day
Voxel domain	Western Austria ($46.4 - 48.0°$ lat, $10.4 - 13.4°$ lon, $h = 0 - 13.6km$)
Voxel size	$0.4°$ lat x $0.6°$ lon (4 x 5 ground voxels), 15 height layers
GNSS data	30 sec dual-frequency GPS and GLONASS observations - obtained from 6
	EPOSA reference sites: SEEF, MATR, JENB, KIBG, ROET, SILL
A priori model	ALARO analysis data of temperature and specific humidity
	- provided on 18 pressure levels in grib1 format for 8 epochs per day
Observations	SWDs for all GPS and GLONASS satellites in view above $3°$
	elevation angle - derived from 1h ZTD and 2h gradient estimates
Ray-tracer	Sol1: Straight line ray-tracing for all observations up to $h = 13.6km$
	Sol2: Straight line ray-tracing for $\varepsilon > 15°$ and bended
	ray-tracing for $\varepsilon \leq 15°$ (mixed approach) up to $h = 13.6km$
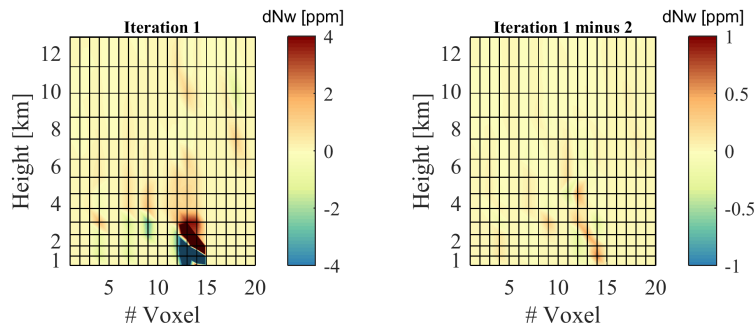
Figure 7. (left): Differences in wet refractivity between straight line and mixed straight line / bended ray-tracing solution, (right): Differences in wet refractivity between first and second iteration (compare also to Fig. 3). Analyzed period: May 4, 2013, 15 UTC

4.1 Validation with radiosonde data

For validation of the mixed ray-tracing approach against straight line ray-tracing, the tomography derived wet refractivity fields were compared with radiosonde data at the airport of Innsbruck ($\varphi_i = 47.3°, \lambda = 11.4°, h = 579m$). First, the radiosonde data obtained once a day between 2 and 3 UTC were pre-processed, i.e. outliers in temperature were removed and dew point temperature was converted to water vapor pressure and further to wet refractivity. Finally, the radiosonde profiles were vertically interpolated to the height layers of the voxel model and the tomography derived wet refractivity fields were horizontally interpolated to the ground-position of the radiosonde launching site, respectively. Figure 8 shows the differences in wet refractivity as function of height above surface, exemplarily for two epochs in May, 2013. In both cases, the bended ray-tracing approach
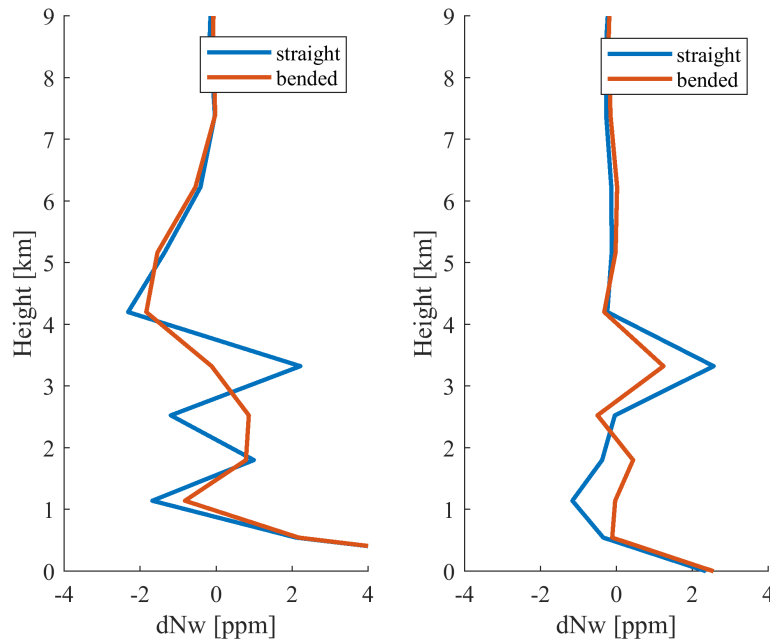
Atmospheric
Measurement
Techniques

Discussions

Figure 8. Differences in wet refractivity between radiosonde and two tomography solutions based on straight line (blue) and bended ray-tracing (red), exemplary for May 1, 2013, 3 UTC (left) and May 31, 3 UTC (right)

helps to reduce the tomography error by about $1-2ppm$, especially in the lower 4 km of the atmosphere. Largest differences are visible when the bended ray traverses other voxels than its chord line. This appeared in about 2 % of the test cases, especially if observations below $10°$ elevation angle enter the tomography solution.

5 Conclusions

5   GNSS signals which enter the neutral atmosphere at low elevation angles ($\varepsilon < 15°$) are significantly affected by atmospheric bending. In case the bending is neglected when setting up design matrix $\boldsymbol{A}$, a systematic error of up to $10-20ppm$, on average of $1-2ppm$ is introduced into the GNSS tomography solution. This error can be widely reduced if atmospheric bending is considered in reconstruction of the signal paths. Therefore, a 2D piecewise linear ray-tracing approach has been defined, which describes the GNSS signal path by small line segments. By limiting the length of the line segments to $100m$ in case of $\varepsilon = 3°$

10   or even shorter for higher elevation angles, the 'true' signal path can be widely reconstructed. However, the quality of the reconstructed signal paths depends primarily on the quality of the a priori refractivity field. Comparisons between refractivity fields derived from standard atmosphere and ALARO weather model data reveal that an a priori refractivity error of $30ppm$ can cause a ray deviation of up to several hundred meters, i.e. the distance traveled in each voxel but also the number of traversed

Atmospheric
Measurement
Techniques
Discussions

voxels is prone to misallocations. In consequence, reliable a priori data, e.g. derived from numerical weather model data, are recommended for GNSS tomography.

Nevertheless, if reliable a priori data are not available or if the quality is unknown, iterative tomography processing helps for reducing the impact of the a priori refractivity field on the tomography solution. Therefore, the refractivity field obtained

5   from an initial tomography solution is introduced as a priori information for the next iteration. The processing is repeated until the tomography solution converges. This ensues usually after 2-3 iterations - dependent on the quality of the a priori data and whether constraints are applied to the a priori field. Thereby, a bending model, like the one provided by Hobiger et al. (2008a) helps to significantly reduce computational cost by describing the remaining bending in the higher atmosphere (above the voxel model). In consequence, the ray-tracer can be stopped right after the reconstructed signal leaves the voxel model. In case of

10   $h_t = 12km$, the number of processing steps is reduced by 85%, which is a tremendous reduction in processing time without significant loss of accuracy.

In contrast, ionospheric bending effects have less impact on the GNSS tomography solution. Even during periods of solar maximum, ray path deviation caused by ionospheric bending is negligible for signals in L-band $(1 - 2GHz)$. However, even if ionospheric bending has no impact on the tomography solution, first and higher order ionospheric effects should be taken into

15   account when processing GNSS phase observations.

Besides, comparisons with radiosonde data revealed that if atmospheric bending effects are considered in GNSS tomography, the quality of the tomography solution can be improved by $1 - 2ppm$. Within the defined test case, especially voxels in the lower $4km$ of the atmosphere benefitted from the applied mixed ray-tracing approach. Due to significant optimization, the mixed ray-tracing approach ensures processing of large tomography test cases in adequate time. A test case with 72 GNSS

20   sites and 7 x 9 x 15 voxels can be processed in less than two minutes. Thus, the developed mixed ray-tracing approach is applicable also in near real-time and therefore well suited for operational purposes.

Code availability. The 2D piecewise linear ray-tracer for GNSS tomography as well as the Radiate ray-tracer are part of the Vienna VLBI and Satellite Software (VieVS) - accessible for registered users. For more details, the reader is referred to http://vievswiki.geo.tuwien.ac.at.

Appendix A: Unmodelled bending effects in the Vienna hydrostatic mapping function

25   In case of VMF1 (Böhm et al., 2006a) or similar mapping concepts, azimuthal asymmetry is not considered and for convenience, only a single hydrostatic mapping coefficient per site (a_h) is determined as follows:

$$a_h = -\frac{mf_h(\varepsilon) \cdot \sin\varepsilon - 1}{\frac{mf_h(\varepsilon)}{\sin\varepsilon + \frac{b_h}{\sin\varepsilon + c_h}} - \frac{1}{1 + \frac{b_h}{1 + c_h}}}. \tag{A1}$$

where b_h is 0.0029, c_h depends on the day of year and latitude and $mf_h(\varepsilon)$ is defined as the ratio between $SHD(3°)$ and ZHD, obtained by ray-tracing through numerical weather model data. For assessing the remaining unmodeled geometric
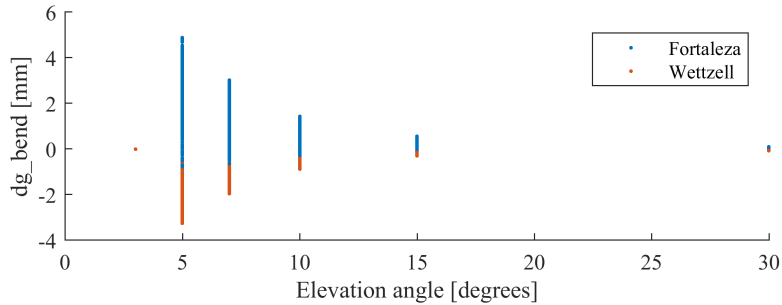
Figure A1. The unmodeled geometric bending effect in VMF1 hydrostatic mapping function (dg_{bend}), exemplary for VLBI sites Fortaleza, Brazil and Wettzell, Germany. Analyzed period: Jan-Feb 2014

bending $dg_{bend}(\varepsilon, \alpha)$, ray-traced slant hydrostatic delays were compared with 'mapped' slant hydrostatic delays as follows:

$$dg_{bend}(\varepsilon, \alpha)[m] = ZHD[m] \cdot mf_h(\varepsilon) - ZHD[m] \cdot mf_{h0}(\varepsilon) - g_{bend}(\varepsilon, \alpha)[m] \tag{A2}$$

where ZHD is the zenith hydrostatic delay obtained by vertical integration, $g_{bend}(\varepsilon, \alpha)$ is the geometric bending effect as obtained by ray-tracing, $mf_h(\varepsilon)$ is the VMF1 hydrostatic mapping function determined by $SHD(3°)/ZHD$ and $mf_{h0}(\varepsilon)$ is the hydrostatic mapping function determined by $SHD_0(3°)/ZHD$, whereby $SHD(3°)$ and $SHD_0(3°)$ are the slant hydrostatic delays obtained by ray-tracing for an outgoing elevation angle $\varepsilon_k = 3°$ with and without geometric bending, respectively. Figure A1 shows the remaining unmodeled geometric bending as obtained for six elevation angles (and 16 equidistant azimuth angles), exemplary for the two VLBI sites Fortaleza, Brazil ($\varphi = -3.9°, \lambda = 321.6°, h = 23m$) and Wettzell, Germany ($\varphi = 49.1°, \lambda = 12.9°, h = 669m$). In case of $\varepsilon = 3°$, almost no bending error is visible since $mf_h(\varepsilon)$ was tuned for this elevation angle. However, for other elevation angles, the unmodeled geometric bending is about 3 % of the slant hydrostatic delay, e.g. up to $\pm 5mm$ at 5° elevation angle. In case of Wettzell, $dg_{bend}(\varepsilon, \alpha)$ is mostly negative, i.e. the 'mapped' SHD is smaller than the observed SHD and vice versa for Fortaleza. So far, these small variations are neglected when using VMF1 hydrostatic mapping function in GNSS signal processing.

14

Atmospheric
Measurement
Techniques
Discussions

References

Aghajany, S. H. and Amerian, Y.: Three dimensional ray tracing technique for tropospheric water vapor tomography using GPS measure-
ments, J. Atmospheric Sol.-Terr. Phys., 164, 81–88, https://doi.org/10.1016/j.jastp.2017.08.003, 2017.

Anderson, D. N., Mendillo, M., and Herniter, B.: A semi-empirical low-latitude ionospheric model, Radio Sci., 32, 292–306, 1987.

5 Bender, M., Stosius, R., Zus, F., Dick, G., Wickert, J., and Raabe, A.: Development of a GNSS water vapour tomography system using
algebraic reconstruction techniques, Adv. Space Res., 47, 886–897, https://doi.org/doi:10.1016/j.asr.2010.09.011, 2011.

Bevis, M., Businger, S., Herring, T. A., Rocken, C., Anthes, R. A., and Ware, R. H.: GPS meteorology: Remote sensing of atmospheric water
vapor using the Global Positioning System, J. Geophys. Res., 97, 15 787–15 801, 1992.

Böhm, J., Werl, B., and Schuh, H.: Troposphere mapping functions for GPS and Very Long Baseline Interferometry from European Centre
10   for Medium-Range Weather Forecasts operational analysis data, J. Geophys. Res., 111, 1–9, 2006a.

Champollion, C., Masson, F., Bouin, M.-N., Walpersdorf, A., Doerflinger, E., Bock, O., and Bealen, J. V.: GPS water vapour tomography:
preliminary results from the ESCOMPTE field experiment, Atm. Res., 74, 21, https://doi.org/10.1016/j.atmosres.2004.04.003, 2005.

Chen, G. and Herring, T. A.: Effects of atmospheric azimuthal asymmetry on the analysis of space geodetic data, J. Geophys. Res., 102,
20 489–20 502, 1997.

15 Flores, A.: Atmospheric tomography using satellite radio signals, Ph.D. thesis, Universitat Politecnica de Catalunya, Departament de Teoria
del Senyal i Comunicacions, http://www.tdx.cat/handle/10803/6881, 1999.

Fritsche, M., Dietrich, R., Knöfel, C., Rülke, A., Vey, S., Rothacher, M., and Steigenberger, P.: GPS meteorology: Remote sensing of
atmospheric water vapor using the Global Positioning System, J. Geophys. Res., 97, 15, https://doi.org/10.1029/2005GL024342, 2005.

Hirahara, K.: Local GPS tropospheric tomography, Earth Planets Space, 52, 935–939, https://doi.org/10.1186/BF03352308, 2000.

20 Hobiger, T., Ichikawa, R., Koyama, Y., and Kondo, T.: Fast and accurate ray-tracing algorithms for real-time space geodetic applications
using numerical weather models, J. Geophys. Res., 113, 1–14, https://doi.org/10.1029/2008JD010503, 2008a.

Hofmeister, A.: Determination of path delays in the atmosphere for geodetic VLBI by means of ray-tracing, Ph.D. thesis, TU Wien, Depart-
ment of Geodesy and Geoinformation, http://repositum.tuwien.ac.at/obvutwhs/content/titleinfo/1370367, 2016.

Iyer, H. and Hirahara, K.: Seismic tomography: Theory and practice, Springer Netherlands, iSBN: 9780412371905, 1993.

25 Landskron, D. and Böhm, J.: Refined discrete and empirical horizontal gradients in VLBI analysis, J. Geod., first online,
https://doi.org/10.1007/s00190-018-1127-1, 2018.

MacMillan, D. S.: Atmospheric gradients from Very Long Baseline Interferometry observations, Geophys. Res. Lett., 22, 1041–1044, 1995.

Möller, G.: Reconstruction of 3D wet refractivity fields in the lower atmosphere along bended GNSS signal paths, Ph.D. thesis, TU Wien,
Department of Geodesy and Geoinformation, http://repositum.tuwien.ac.at/obvutwhs/content/titleinfo/2268559, 2017.

30 Nievinski, F. G.: Ray-tracing Options to Mitigate the Neutral Atmosphere Delay in GPS, Master's thesis, 2009.

Raymond, T. D., Franke, S. J., and Yeh, K. C.: Ionospheric tomography: its limitations and reconstruction methods, J. Atmospheric Terr.
Phys., 56, 637–657, https://doi.org/10.1016/0021-9169(94)90104-X, 1994.

Wijaya, D. D.: Atmospheric correction formulae for space geodetic techniques, Shaker Verlag GmbH, Germany, https://www.amazon.
com/Atmospheric-Correction-Formulae-Techniques-Engineering/dp/3832289941?SubscriptionId=0JYN1NVW651KCA56C102&tag=
35   techkie-20&linkCode=xm2&camp=2025&creative=165953&creativeASIN=3832289941, 2010.